Nano Research
2019, 12(4): 919–924

ISSN 1998-0124 CN 11-5974/O4
https://doi.org/10.1007/s12274-019-2323-x

Research Article

Hexagonal boron nitride nanosheet for effective ambient N_2 fixation to NH_3

Ya Zhang[1,§], Huitong Du[2,§], Yongjun Ma[3], Lei Ji[1], Haoran Guo[4], Ziqi Tian[4], Hongyu Chen[1], Hong Huang[1], Guanwei Cui[5], Abdullah M. Asiri[6], Fengli Qu[3] (✉), Liang Chen[4] (✉), and Xuping Sun[1] (✉)

[1] *Institute of Fundamental and Frontier Sciences, University of Electronic Science and Technology of China, Chengdu 610054, China*
[2] *College of Chemistry and Chemical Engineering, Qufu Normal University, Qufu 273165, China*
[3] *Analytical and Test Center, Southwest University of Science and Technology, Mianyang 621010, China*
[4] *Ningbo Institute of Materials Technology and Engineering, Chinese Academy of Sciences, Ningbo 315201, China*
[5] *College of Chemistry, Chemical Engineering and Materials Science, Shandong Normal University, Jinan 250014, China*
[6] *Chemistry Department, Faculty of Science & Center of Excellence for Advanced Materials Research, King Abdulaziz University, P.O. Box 80203, Jeddah 21589, Saudi Arabia*
§ *Ya Zhang and Huitong Du contributed equally to this work.*

Received: 23 November 2018 / **Revised:** 13 January 2019 / **Accepted:** 29 January 2019

ABSTRACT

Industrial production of NH_3 from N_2 and H_2 significantly relies on Haber–Bosch process, which suffers from high energy consume and CO_2 emission. As a sustainable and environmentally-benign alternative process, electrochemical artificial N_2 fixation at ambient conditions, however, is highly required efficient electrocatalysts. In this study, we demonstrate that hexagonal boron nitride nanosheet (h-BNNS) is able to electrochemically catalyze N_2 to NH_3. In acidic solution, h-BNNS catalyst attains a high NH_3 formation rate of 22.4 $\mu g \cdot h^{-1} \cdot mg^{-1}_{cat.}$ and a high Faradic efficiency of 4.7% at −0.75 V vs. reversible hydrogen electrode, with excellent stability and durability. Density functional theory calculations reveal that unsaturated boron at the edge site can activate inert N_2 molecule and significantly reduce the energy barrier for NH_3 formation.

KEYWORDS

boron nitride nanosheet, N_2 reduction reaction, NH_3 electrosynthesis, ambient conditions, density functional theory

1 Introduction

NH_3, an activated nitrogen building block, is essential in manufacturing medicaments, fertilizers, resins, dyes, and explosives [1–3], and it is also regarded as a hydrogen storage molecule featuring no CO_2 emission but having high energy density [4]. N_2 is rather unactive [5] because of its low polarizability, strongest N≡N triple bond, and lack of a dipole moment [6, 7]. Yet N_2 does undergo chemical transformations and industrially produced NH_3 mainly depends on Haber–Bosch method processed N_2 and H_2 molecules at high temperatures and pressures [8]. However, the harsh conditions render this reaction rather energy-intensive and the production of high-purity H_2 gas for the process also causes significant CO_2 evolution [9]. It is thus highly attractive to explore environmentally-benign process for NH_3 synthesis with less energy consumption.

N_2 is biologically fixed by natural enzyme in bacteria at atmospheric pressure and ambient temperature to produce NH_3 [10–12]. Electrochemical synthesis of NH_3 could also provide an alternative and environmentally-benign approach at ambient conditions while it is imperative to develop high-performance electrocatalysts for the N_2 reduction reaction (NRR) [13–15]. It is well known that noble-metal catalysts show superior performance toward NRR [16–20], but their high price and scarcity inhibit industrial applications. Encouragingly, much progress has also been made in exploring non-precious metal NRR catalysts [21–32]. On the other hand, utilizing metal-free catalysts can significantly avoid the release of metal ions and thus reduce the environmental impact. Zhao group reported the use of N-doped porous carbon as a metal-free electrocatalyst with impressive NH_3 yield (V_{NH_3}) of 23.8 $\mu g \cdot h^{-1} \cdot mg^{-1}_{cat.}$, but it only achieves a low Faradaic efficiency (FE) of 1.42% [33].

Two-dimensional (2D) nanomaterials are a center of interest owing to the large surface areas suitable for catalytic applications. With the discovery of the unique properties of graphene [34, 35], 2D layered materials like transition metal chalcogenides and oxides as well as other 2D compounds have stimulated great interests in recent years [36–41]. Featuring by its exotic properties including high mechanical strength, high thermal conductivity, chemical stability, and high electrical resistance, 2D hexagonal boron nitride (h-BN) has been widely used in field effect transistors, tunneling devices, deep UV emitters and detectors, photoelectric devices, and nanofillers, etc. [42]. Although it has a wide band gap [43], the band gap of the h-BN monolayer can be significantly reduced by B-, N-vacancies and impurity defects [44]. Thus, ultrathin h-BN layers own narrowed band gap and improved conductivity tuned by a transverse electric field or edge structure [45–47]. Moreover, electronic communication to h-BN surface is established via electron tunneling through ultrathin h-BN layers [48]. We anticipate that h-BN nanosheet (h-BNNS) has the potential to electrochemically catalyze NRR, which, however, has never been explored before.

In this communicaton, we demonstrate that h-BNNS works

Address correspondence to Xuping Sun, xpsun@uestc.edu.cn; Fengli Qu, fengliquhn@hotmail.com; Liang Chen, chenliang@nimte.ac.cn

as a highly active electrocatalyst for converting N_2 to NH_3 at room temperature and pressure. The h-BNNS attains a high V_{NH_3} of 22.4 μg·h^{-1}·mg$^{-1}_{cat.}$ and FE of 4.7% at −0.75 V vs. reversible hydrogen electrode (RHE) in 0.1 M HCl. Density functional theory (DFT) calculations further show that the unsaturated boron at the edge site is capable of activating inert N_2 molecule and significantly reducing the energy barrier for NH_3 formation.

2 Experimental

2.1 Sample preparation

h-BNNS was synthesized by liquid exfoliation of bulk h-BN powders [49, 50]. Typically, 100 mg bulk h-BN powders were dispersed in 10 mL ethanol and exfoliated by ultrasonic cell disruptor. Then, the exfoliated solution containing bulk h-BN and h-BNNS was collected and subjected to centrifugation at 6,000 rpm for 10 min. Finally, the resulting supernatant solution containing the h-BNNS with the concentration about 0.6 mg·mL^{-1} was collected. 10 mg as-prepared h-BNNS were dispersed in 1 mL ethanol, 480 μL ethanol containing 20 μL of 5 wt.% Nafion was added into 500 μL obtained solution sonicated for 1 h. 20 μL inks was loaded on a 1 cm × 1 cm carbon paper and dried.

2.2 Characterizations

XRD patterns were performed by SHIMADZU LabX XRD-6100. SEM images were recorded using a Hitachi S-4800 scanning electron microscope operated at 20 kV. AFM data were recorded using Bruker MultiMode-8 atomic force microscopy (Bruker, USA). TEM characterization was acquired to use HITACHI H-8100 electron microscopy (Hitachi, Tokyo, Japan) with operating at 200 kV. The ion chromatography data were collected by Swiss Wangtong ECO with conductivity detector. The gaseous product was detected by a gas chromatograph (GC; Shimadzu, GC-2014) with a thermal conductivity detector (TCD) for H_2. Determination of NH_4^+ by ion chromatography was carried out by using the chromatographic column of wantong C-4 at 35 °C with 20 μL sample. UV–Vis diffuse reflectance spectra were performed on SHIMADZU UV-1800 UV–Vis spectrophotometer. The obtained $^{15}NH_4^+$ was measured using ^{1}H NMR spectroscopy (Bruker AVANCE III 500 HD). XPS data were collected on an ESCALABMK II X-ray photoelectron spectrometer.

2.3 Electrochemical measurements

To examine the catalytic activity for N_2 reduction, electrochemical experiments were measured on a CH Instruments 660E, with two-compartment three-electrode electrochemical cell (Ag/AgCl electrode, h-BNNS/CP and a graphite rod were used as reference electrode, working electrode and counter electrode, respectively). All measured potentials were converted into a RHE scale

$$E\ (\text{vs. RHE}) = 0.197\ \text{V} + 0.059 \times \text{pH} + E\ (\text{vs. Ag/AgCl})$$

To evaluate the effect of surface area, the ECSA of h-BNNS/CP and bulk h-BN/CP were measured by CV with different scan rates. By plotting the $\Delta J = (J_a - J_c)$ against the scan rate, the twice of the double layer capacitance (C_{dl}) is obtained, which corresponds to its linear slope in Fig. S3 in the Electronic Supplementary Material (ESM). Based on the reported method, we use specific capacitances of C_s = 0.04 mF·cm^{-2} (typical reported value) to estimate of ECSA of various electrodes (ECSA = C_{dl}/C_s) [51–53].

2.4 Quantitative detection NH_3

NH_3 concentration was calculated by indophenol blue method [54]. 2 mL of 1 M NaOH solution containing sodium citrate (5 wt.%) and salicylic acid (5 wt.%), 1 mL of 50 mM NaClO and 0.2 mL of $Na_2Fe(CN)_5NO{\cdot}2H_2O$ (1 wt.%) droped successively in 2 mL electrolyte from cathodic chamber. After 2 h standing at room temperature, the absorbance of test solutions in a glass cuvette was measured at 655 nm. The fitting curve presents excellent positive correlation ($y = 1.287x + 0.068$, $R^2 = 0.999$) between absorbance value and NH_4^+ concentrations.

2.5 Quantitative detection of N_2H_4

The concentration of N_2H_4 was quantitatively detected according to previous work [55]. To prepare sensitive chromogenic reagent, 5.99 g para(dimethylamino)benzaldehyde was dissolved in 30 mL concentrated HCl containing 300 mL ethanol. The absorbance of N_2H_4 after mixing with the chromogenic reagent in the resulting electrolyte was estimated at 455 nm. The fitting curve displays excellent positive correlation ($y = 1.009x + 0.0455$, $R^2 = 0.998$) between absorbance value and NH_4^+ concentrations.

2.6 Calculation of the FE and V_{NH_3}

Calculation of the FE

$$\text{FE} = \frac{3F \times V \times [\text{NH}_3]}{Q \times 17}$$

Rate of NH_3 formation was calculated

$$V_{\text{NH}_3} = \frac{V \times [\text{NH}_3]}{m_{\text{cat.}} \times t}$$

Where $[NH_3]$ is obtained NH_3 concentration; F is the Faraday constant; Q is the quantity of applied electricity; $m_{cat.}$ is catalyst mass; V is the volume of electrolyte for NH_3 detection; t is the reduction time. The Q and V for this study are listed in Table S1 in the ESM.

2.7 Calculation details

The first-principles calculations were carried out using Viena *Ab initio* software package (VASP) [56] to investigate NRR on the zigzag edge of BN. Calculations were based on DFT with the generalized gradient approximation (GGA) of Perdew–Burke–Eznerhof (PBE) functional [57]. The Projector Augmented Wave (PAW) potentials [58] were used to describe electron interaction. Slab model was constructed in 3 × 3 × 1 supercell. To avoid interaction of neighboring slab, a 20 Å vacuum was introduced along the z axis. To simulate the surface system, the top four layers with adsorbed molecular were relaxed and other layers were fixed. Energy cutoff for plane wave-basis was set as 450 eV, and the threshold of geometry relaxation was 0.005 eV·Å^{-1} in force. A 2 × 2 × 1 Monkhorst–Pack k-point mesh was used to sample the Brillouin zone. Van der Waals interaction was also considered using empirical DFT-D3 correction [59].

3 Results and discussion

h-BNNS was prepared by liquid exfoliation from bulk h-BN powders [49, 50]. X-ray diffraction (XRD) patterns of bulk h-BN powder and its exfoliated product are exhibited in Fig. 1(a). The diffraction peaks of bulk h-BN powders match well with h-BN (JCPDS No. 45-0893). Exfoliated product shows peaks at 26.7°, 41.5°, 50.0°, and 54.9° with a lower intensity, indicating the formation of h-BNNS [60, 61]. Figure S1 in the ESM and Fig. 1(b) display scanning electron microscopy (SEM) and transmission electron microscopy (TEM) of bulk h-BN and h-BNNS, respectively, further verifying the formation of untrathin nanosheet after liquid exfoliation. Atomic force microscope image and corresponding height profile (Fig. 1(c)) show that h-BNNS owns an average thickness about 1.3 nm. The high-resolution TEM (HRTEM) image (Fig. 1(d)) recorded on such nanosheet reveals the measured interlayer distance of 0.22 nm, which should be assigned to the (100) plane of h-BN. Figure S2 in

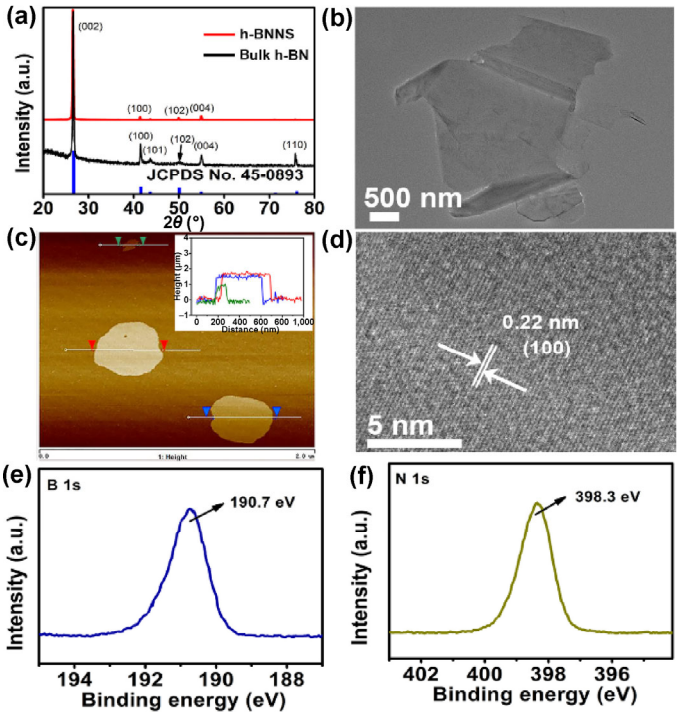

Figure 1 (a) XRD pattern for bulk h-BN and h-BNNS. (b) TEM image for h-BNNS. (c) AFM image and corresponding height profile for h-BNNS. (d) HRTEM image for h-BNNS. The regions (e) B 1s and (f) N 1s from XPS spectra of h-BNNS.

the ESM gives X-ray photoelectron spectroscopy survey spectrum of h-BNNS, with the detected elements of B and N. As observed in Fig. 1(e), the peak at 190.7 eV is assigned to the B 1s region, which is attributed to B atoms surrounded only by N atoms [62]. The N 1s peak (Fig. 1(f)) near 398.3 eV can be related to N atoms in N–B bonds [63].

To evaluate electrocatalytic NRR performance, h-BNNS was deposited on carbon paper (h-BNNS/CP; h-BNNS loading: 0.1 mg·cm^{-2}) and tested in 0.1 M HCl aqueous solution, which provides more protons for the NRR. All potentials were converted to the RHE scale. N_2 gas was continuously fed into cathodic compartment during electrolysis. Linear sweep voltammetry curves of h-BNNS/CP and bulk h-BN/CP with electrochemical active surface area (ECSA) (Fig. S3 in the ESM) normalized in N_2- and Ar-saturated solution are shown in Fig. S4 in the ESM. From ECSA normalized performance of h-BNNS/CP and bulk h-BN/CP, the high catalytic activity of h-BNNS/CP includes an appreciable intrinsic (not surface-area-related) contribution [51], which relates to the unsaturated boron at active zigzag edge of layered structure [64].

Figure 2(a) shows time-dependent current density curves at various potentials with satisfactory stability. The current density starts high and then levels off, which may be attributed to the charging of double-layer as well as local concentration reducing of H^+ and N_2 near the electrode surface [27, 65]. To identify the ability of h-BNNS/CP for NRR, both produced NH_3 and N_2H_4 were detected after electrolysis, and NH_3 concentrations were analyzed and quantified by the indophenol blue method [54] and ion chromatography, while N_2H_4 was quantitatively detected according to previous work [55]. Figures S5 and S6 in the ESM show corresponding calibration curves, respectively. The absorbance derived from UV–Vis spectra after each potentiostatic test (Fig. 2(b)), indicating that electrocatalytic NRR process occurs from the range of −0.65 to −1.05 V. Both V_{NH_3} and FEs at different potentials are then measured in Fig. 2(c). The V_{NH_3} and FEs increase from −0.65 to −0.75 V and then decrease with potential becoming more negative. Strikingly, V_{NH_3} and FE reach a maximum value of 22.4 μg·h^{-1}·mg$^{-1}_{cat.}$ and 4.7%, respectively.

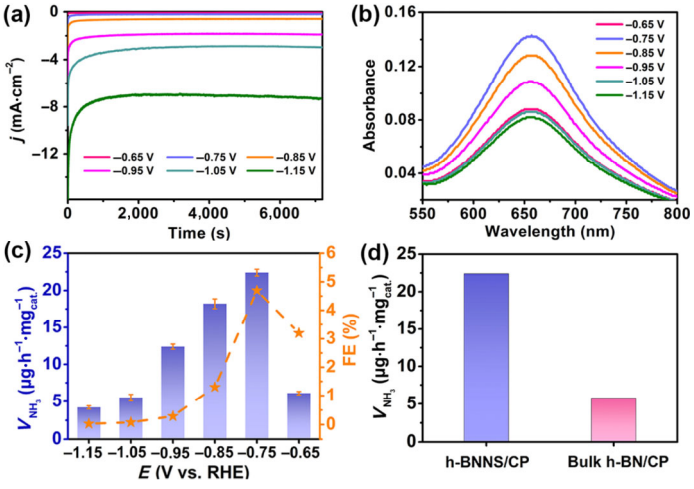

Figure 2 (a) Chronoamperometry results of h-BNNS/CP at various potentials. (b) UV–Vis curves for the electrolytes colored by indophenol after electrolysis 2 h at each given potential. (c) V_{NH_3} and FEs for h-BNNS/CP at each given potential. (d) The NH_3 yields for various electrodes at −0.75 V after electrolysis 2 h.

This results are almost confirmed by the detection of ion chromatography (Fig. S7 and Table S2 in the ESM). The V_{NH_3} is superior to most reported NRR catalysts, such as S-doped carbon nanosphere (19.07 μg·h^{-1}·mg$^{-1}_{cat.}$) [66], γ-Fe_2O_3 (0.2 μg·h^{-1}·mg$^{-1}_{cat.}$) [67] and Au nanorods (6.0 μg·h^{-1}·mg$^{-1}_{cat.}$) [16]. Table S3 in the ESM lists more detailed comparison. When the potential is below −0.75 V, both NH_3 yield and FEs decrease due to the apparent competing reaction caused by HER (Fig. S8 in the ESM) [16, 27, 68]. N_2H_4 is not detected (Fig. S9 in the ESM), indicating this catalyst possesses excellent selectivity.

In order to ensure that existing NH_3 is only obtained from the NRR process of h-BNNS/CP, we also performed two control experiments: immersing samples in N_2-saturated solution without applied voltage for 2 h and immersing samples in Ar-saturated solution at −0.75 V for 2 h. Figure S10 in the ESM displays corresponding absorbance derived from UV–Vis spectra, proving the accuracy of experimental operation and eliminating background contributions. ^{15}N isotopic labeling experiment was also carried out to prove that h-BNNS can efficiently transfer N_2 into NH_3. The ^1H NMR spectra reveal that only $^{15}NH_4^+$ was detected when $^{15}N_2$ as feeding gas (Fig. S11 in the ESM). It is thus safe to conclude that h-BNNS is robust enough to stand for electrolysis in acids and that the detected NH_3 only originates from electrocatalytic hydrogenation of N_2. NRR activities of bare CP and bulk h-BN coated on CP with the same loading (bulk h-BN/CP) were also tested. Clearly, bare CP exhibits poor performance for electrocatalytic NRR (Fig. S12 in the ESM). It is worth noting that bulk h-BN/CP can effectively catalyze N_2 with the V_{NH_3} of 5.7 μg·h^{-1}·mg$^{-1}_{cat.}$ in Fig. 2(d). In sharp contrast, h-BNNS/CP shows greatly enhanced NRR activity (22.4 μg·h^{-1}·mg$^{-1}_{cat.}$). The superior activity for h-BNNS/CP can be reasonably ascribe to that ultrathin nature of h-BNNS leads to excellent electronic communication between h-BNNS and CP through electron tunneling [44]. Indeed, Nyquist plots of h-BNNS/CP and bulk h-BN/CP (Fig. S13 in the ESM) suggest that h-BNNS/CP has a lower charge transfer resistance [69] and thus results in fast charge transfer to achieve a higher NH_3 yield rate.

Stability and durability of an electrocatalyst are also critical for practical applications. Consecutive six recycling tests at −0.75 V show ignorable variation in V_{NH_3} and FE (Fig. 3(a)). The current density is only slightly decreased after 24 h electrolysis (Fig. 3(b)). The h-BNNS still maintains its nanosheet morphology (Fig. S14 in the ESM) and is also hexagonal boron nitride in nature (Figs. S15 and S16 in the ESM) after long-term NRR electrolysis, further

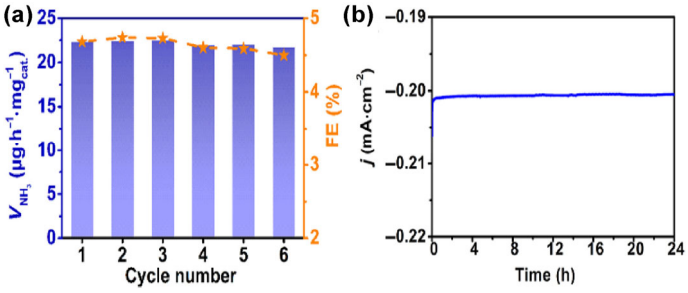

Figure 3 (a) Recycling test and (b) chronoamperometry results of h-BNNS/CP at –0.75 V.

confirming it has strong robustness against NRR electrolysis under strongly acidic reaction conditions. All these results show that h-BNNS has good stability and durability. The NRR activity of h-BNNS/CP after durability test was further tested. As shown in Fig. S17 in the ESM, the intensity of absorbance for the electrolyte is almost the same as that shown in Fig. 2(b), indicating h-BNNS still is highly active toward electrosynthesis NH_3. So h-BNNS is robust enough to stand for the NRR electrolysis due to its intrinsic high mechanical strength and chemical stability [42].

We carried out DFT calculations to investigate the catalytic mechanism. As observed in experiments, the (100) surface of h-BNNS was exposed, which relates to the unsaturated boron at active zigzag edge of layered structure. Based on computational hydrogen electrode model (CHE) [70], we calculated and plotted free energy profile of NRR in Fig. 4, in which the asterisk (*) denotes the adsorption state. Interestingly, N_2 can readily form a 5-membered ring at the edge site. Actually, we attempted to locate the structure of physisorbed N_2. However, once N_2 approaches the unsaturated boron atoms, a [3+2] cycloaddition would take place. We plotted the charge density as well as the electrostatic potential of the h-BNNS in Fig. 4(b), showing

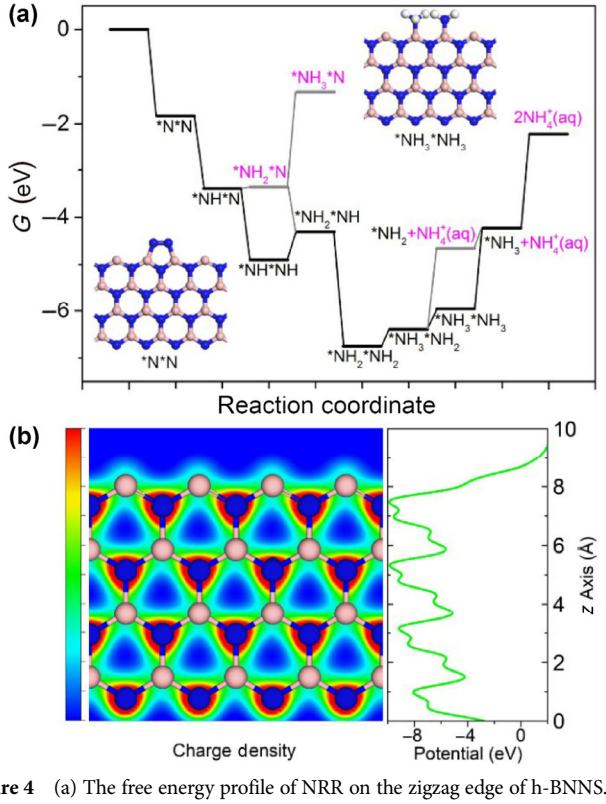

Figure 4 (a) The free energy profile of NRR on the zigzag edge of h-BNNS. The key intermediates are shown in insets. (b) The charge density from the side view. Red and cyan represent high and low electron density, respectively. Electrostatic potential on *z*-direction is shown for comparison. Colour code: blue, N; pink, B; white, H.

that electron accumulates on nitrogen while the boron on the edge is electron deficient. The orbital of boron possesses few valence electron that can accept electrons from π-orbital of nitrogen, resulting in feasible chemisorption of the inert molecule. Subsequently, we examined both distal and enzymatic dissociative pathways. Similar to the NRR process catalyzed by BN-supported single-Mo atom [71], the enzymatic mechanism is found to be energetically favourable. The potential determining step was identified as the reaction from *NH*NH to *NH_2*NH, with energy barrier of 0.60 eV. Thus, electroreduction of N_2 can theoretically occur at an external potential of –0.60 V, in good agreement with the experimental result. Considering the acidic condition in experiment, hydrated NH_4^+ cation (NH_4^+ (aq)) would desorb from the edge rather than NH_3 gas. We have to mention that desorption of NH_4^+ from edge sites requires much more energy than the proton-electron coupling reduction. The high energy barriers for the first and second cation desorption are 1.73 and 2.01 eV, respectively, which may affect the electrochemical onset potential a little, but significantly slow down the reaction kinetic. Here we suppose that cation desorption can couple with intense water adsorption to the surface. The calculated free energy of water sorption is –2.08 eV. As a result, desorption free energies decrease to –0.25 and –0.11 eV, respectively. On the other hand, strong water adsorption to the surface might also occupy the active sites to hinder N_2 adsorption. Considering the intense adsorption between N_2 and the edge with binding energy of –1.83 eV and significant accumulation of free energy from *N*N to *NH*NH (–4.90 eV), the overall process should still be energetically efficient, as suggested in other previous studies [5, 27].

4 Conclusions

In summary, h-BNNS is proven as a robust metal-free electrocatalyst for NH_3 synthesis at ambient conditions. It attains a high FE (4.7%) and a high V_{NH_3} (22.4 μg·h^{-1}·mg$^{-1}_{cat.}$) at –0.75 V vs. RHE in acidic solution. DFT calculations suggest that the unsaturated boron at the edge site can activate inert N_2 molecule and dramatically reduce the energy barrier for NH_3 formation. This work not only offers us an attractive electrocatalyst for NH_3 production, but would motivate more research efforts to further explore the potential of BN-based nanocatalysts for artificial N_2 fixation.

Acknowledgements

This work was supported by the National Natural Science Foundation of China (Nos. 21575137, 21775089, and 21375076), the Key Research and Development Program of Shandong Province (No. 2015GSF121031) and the Natural Science Foundation Projects of Shandong Province (Nos. ZR2017JL010, ZR2017QB008, and ZR2017LEE006).

Electronic Supplementary Material: Supplementary material (SEM and TEM images; XPS, UV–Vis absorption, GC and ^{1}H NMR spectra; calibration and chrono-amperometry curves; LSV curves; NH_3 and N_2H_4 yields; FEs; Nyquist plots; XRD pattern; Tables S1–S3) is available in the online version of this article at https://doi.org/10.1007/s12274-019-2323-x.

References

[1] Smil, V. Detonator of the population explosion. *Nature* **1999**, *400*, 415.
[2] Schlögl, R. Catalytic synthesis of ammonia—A "never-ending story"? *Angew. Chem., Int. Ed.* **2003**, *42*, 2004–2008.
[3] Rosca, V.; Duca, M.; De Groot, M. T.; Koper, M. T. M. Nitrogen cycle electrocatalysis. *Chem. Rev.* **2009**, *109*, 2209–2244.
[4] Vegge, T.; Sørensen, R. Z.; Klerke, A.; Hummelshøj, J. S.; Johannessen, T.; Nørskov, J. K.; Christensen, C. H. Indirect hydrogen storage in metal ammines. In *Solid-State Hydrogen Storage*; Walker, G., Ed.; Woodhead Publishing Limited: Cambridge, 2008; pp 533–564.

[5] Ling, C. Y.; Niu, X. H.; Li, Q.; Du, A. J.; Wang, J. L. Metal-free single atom catalyst for N_2 fixation driven by visible light. *J. Am. Chem. Soc.* **2018**, *140*, 14161–14168.

[6] Fryzuk, M. D.; Love, J. B.; Rettig, S. J.; Young, V. G. Transformation of coordinated dinitrogen by reaction with dihydrogen and primary silanes. *Science* **1997**, *275*, 1445–1447.

[7] Singh, A. R.; Rohr, B. A.; Schwalbe, J. A.; Cargnello, M.; Chan, K.; Jaramillo, T. F.; Chorkendorff, I.; Nørskov, J. K. Electrochemical ammonia synthesis—The selectivity challenge. *ACS Catal.* **2017**, *7*, 706–709.

[8] Jennings, J. R. *Catalytic Ammonia Synthesis*; Plenum: New York, 1991.

[9] Dybkjaer, I. Ammonia production processes. In *Ammonia*: *Catalysis and Manufacture*. Nielsen, A., Ed.; Springer: Berlin, Heidelberg, 1995; pp 199−327.

[10] Chan, M. K.; Kim, J.; Rees, D. C. The nitrogenase FeMo-cofactor and P-cluster pair: 2.2 a resolution structures. *Science* **1993**, *260*, 792–794.

[11] Burgess, B. K.; Lowe, D. J. Mechanism of molybdenum nitrogenase. *Chem. Rev.* **1996**, *96*, 2983–3011.

[12] Brown, K. A.; Harris, D. F.; Wilker, M. B.; Rasmussen, A.; Khadka, N.; Hamby, H.; Keable, S.; Dukovic, G.; Peters, J. W.; Seefeldt, L. C.; King, P. W. Light-driven dinitrogen reduction catalyzed by a CdS: Nitrogenase MoFe protein biohybrid. *Science* **2016**, *352*, 448–450.

[13] Seh, Z. W.; Kibsgaard, J.; Dickens, C. F.; Chorkendorff, I.; Nørskov, J. K.; Jaramillo, T. F. Combining theory and experiment in electrocatalysis: Insights into materials design. *Science* **2017**, *355*, eaad4998.

[14] Guo, C. X.; Ran, J. R.; Vasileff, A.; Qiao, S. Z. Rational design of electrocatalysts and photo(electro)catalysts for nitrogen reduction to ammonia (NH_3) under ambient conditions. *Energy Environ. Sci.* **2018**, *11*, 45–56.

[15] Cao, N.; Zheng, G. F. Aqueous electrocatalytic N_2 reduction under ambient conditions. *Nano Res.* **2018**, *11*, 2992–3008.

[16] Bao, D.; Zhang, Q.; Meng, F. L.; Zhong, H. X.; Shi, M. M.; Zhang, Y.; Yan, J. M.; Jiang, Q.; Zhang, X. B. Electrochemical reduction of N_2 under ambient conditions for artificial N_2 fixation and renewable energy storage using N_2/NH_3 cycle. *Adv. Mater.* **2017**, *29*, 1604799.

[17] Nazemi, M.; Panikkanvalappil, S. R.; El-Sayed, M. A. Enhancing the rate of electrochemical nitrogen reduction reaction for ammonia synthesis under ambient conditions using hollow gold nanocages. *Nano Energy* **2018**, *49*, 316–323.

[18] Kordali, V.; Kyriacou, G.; Lambrou, C. Electrochemical synthesis of ammonia at atmospheric pressure and low temperature in a solid polymer electrolyte cell. *Chem. Commun.* **2000**, 1673–1674.

[19] Kordali, V.; Kyriacou, G.; Lambrou, C. Electrochemical synthesis of ammonia at atmospheric pressure and low temperature in a solid polymer electrolyte cell. *Chem. Commun.* **2000**, 1673−1674.

[20] Huang, H. H.; Xia, L.; Shi, X. F.; Asiri, A. M.; Sun, X. P. Ag nanosheets for efficient electrocatalytic N_2 fixation to NH_3 under ambient conditions. *Chem. Commun.* **2018**, *54*, 11427–11430.

[21] Chen, S. M.; Perathoner, S.; Ampelli, C.; Mebrahtu, C.; Su, D. S.; Centi, G. Electrocatalytic synthesis of ammonia at room temperature and atmospheric pressure from water and nitrogen on a carbon-nanotube-based electrocatalyst. *Angew. Chem., Int. Ed.* **2017**, *56*, 2699–2703.

[22] Chen, S. M.; Perathoner, S.; Ampelli, C.; Mebrahtu, C.; Su, D. S.; Centi, G. Room-temperature electrocatalytic synthesis of NH_3 from H_2O and N_2 in a gas-liquid-solid three-phase reactor. *ACS Sustainable Chem. Eng.* **2017**, *5*, 7393–7400.

[23] Yang, D. S.; Chen, T.; Wang, Z. J. Electrochemical reduction of aqueous nitrogen (N_2) at a low overpotential on (110)-oriented Mo nanofilm. *J. Mater. Chem. A* **2017**, *5*, 18967–18971.

[24] Lv, C.; Yan, C. S.; Chen, G.; Ding, Y.; Sun, J. X.; Zhou, Y. S.; Yu, G. H. An amorphous noble-metal-free electrocatalyst that enables nitrogen fixation under ambient conditions. *Angew. Chem., Int. Ed.* **2018**, *57*, 6073−6076.

[25] Liu, Q.; Zhang, X. X.; Zhang, B.; Luo, Y. L.; Cui, G. W.; Xie, F. Y.; Sun, X. P. Ambient N_2 fixation to NH_3 Electrocatalyzed by a spinel Fe_3O_4 nanorod. *Nanoscale* **2018**, *10*, 14386–14389.

[26] Zhang, R.; Zhang, Y.; Ren, X.; Cui, G. W.; Asiri, A. M.; Zheng, B. Z.; Sun, X. P. High-efficiency electrosynthesis of ammonia with high selectivity under ambient conditions enabled by VN nanosheet array. *ACS Sustainable Chem. Eng.* **2018,** *6*, 9545–9549.

[27] Qiu, W. B.; Xie, X. Y.; Qiu, J. D.; Fang, W. H.; Liang, R. P.; Ren, X.; Ji, X. Q.; Cui, G. W.; Asiri, A. M.; Cui, G. L.; Tang, B.; Sun, X. P. High-performance artificial nitrogen fixation at ambient conditions using a metal-free electrocatalyst. *Nat. Commun.* **2018**, *9*, 3485.

[28] Han, J. R.; Liu, Z. C.; Ma, Y. J.; Cui, G. W.; Xie, F. Y.; Wang, F. X.; Wu, Y. P.; Gao, S. Y.; Xu, Y. H.; Sun, X. P. Ambient N_2 fixation to NH_3 at ambient conditions: Using Nb_2O_5 nanofiber as a high-performance electrocatalyst. *Nano Energy* **2018**, *52*, 264–270.

[29] Zhang, Y.; Qiu, W. B.; Ma, Y. J.; Luo, Y. L.; Tian, Z. Q.; Cui, G. W.; Xie, F. Y.; Chen, L.; Li, T. S.; Sun, X. P. High-performance electrohydrogenation of N_2 to NH_3 catalyzed by multishelled hollow Cr_2O_3 microspheres under ambient conditions. *ACS Catal.* **2018**, *8*, 8540–8544.

[30] Zhang, L.; Ji, X. Q.; Ren, X.; Luo, Y. L.; Shi, X. F.; Asiri, A. M.; Zheng, B. Z.; Sun, X. P. Efficient electrochemical N_2 reduction to NH_3 on MoN nanosheets array under ambient conditions. *ACS Sustainable Chem. Eng.* **2018**, *6*, 9550–9554.

[31] Li, X. H.; Li, T. S.; Ma, Y. J.; Wei, Q.; Qiu, W. B.; Guo, H. R.; Shi, X. F.; Zhang, P.; Asiri, A. M.; Chen, L.; Tang, B.; Sun, X. P. Boosted electrocatalytic N_2 reduction to NH_3 by defect-rich MoS_2 nanoflower. *Adv. Energy Mater.* **2018**, *8*, 1801357.

[32] Wang, Z.; Gong, F.; Zhang, L.; Wang, R.; Ji, L.; Liu, Q.; Luo, Y. L.; Guo, H. R.; Li, Y. H.; Gao, P.; Shi, X. F.; Li, B. H.; Tang, B.; Sun, X. P. Electrocatalytic hydrogenation of N_2 to NH_3 by MnO: Experimental and theoretical investigations. *Adv. Sci.* **2018**, *5*, 1801182.

[33] Liu, Y. M.; Su, Y.; Quan, X.; Fan, X. F.; Chen, S.; Yu, H. T.; Zhao, H. M.; Zhang, Y. B.; Zhao, J. J. Facile ammonia synthesis from electrocatalytic N_2 reduction under ambient conditions on N-doped porous carbon. *ACS Catal.* **2018**, *8*, 1186−1191.

[34] Novoselov, K. S.; Geim, A. K.; Morozov, S. V.; Jiang, D.; Zhang, Y.; Dubonos, S. V.; Grigorieva, I. V.; Firsov, A. A. Electric field effect in atomically thin carbon films. *Science* **2004**, *306*, 666–669.

[35] Mirehi, A.; Heidari-Semiromi, E. Effects of the interplay between electron-electron interaction and intrinsic spin-orbit interaction on the indirect RKKY coupling in graphene nanoflakes. *Phys. Chem. Chem. Phys.* **2019**, *21*, 1324–1335.

[36] Coleman, J. N.; Lotya, M.; O'Neill, A.; Bergin, S. D.; King, P. J.; Khan, U.; Young, K.; Gaucher, A.; De, S.; Smith, R. J. et al. Two-dimensional nanosheets produced by liquid exfoliation of layered materials. *Science* **2011**, *331*, 568–571.

[37] Xu, M. S.; Liang, T.; Shi, M. M.; Chen, H. Z. Graphene-like two-dimensional materials. *Chem. Rev.* **2013**, *113*, 3766–3798.

[38] Sun, Y. F.; Gao, S.; Lei, F. C.; Xie, Y. Atomically-thin two-dimensional sheets for understanding active sites in catalysis. *Chem. Soc. Rev.* **2015**, *44*, 623–636.

[39] Chen, Y.; Tan, C. L.; Zhang, H.; Wang, L. Z. Two-dimensional graphene analogues for biomedical applications. *Chem. Soc. Rev.* **2015**, *44*, 2681–2701.

[40] Zhang, Z. H.; Penev, E. S.; Yakobson, B. I. Two-dimensional boron: Structures, properties and applications. *Chem. Soc. Rev.* **2017**, *46*, 6746–6763.

[41] Kong, X. K.; Liu, Q. C.; Zhang, C. L.; Peng, Z. M.; Chen, Q. W. Elemental two-dimensional nanosheets beyond graphene. *Chem. Soc. Rev.* **2017**, *46*, 2127–2157.

[42] Zhang, K. L.; Feng, Y. L.; Wang, F.; Yang, Z. C.; Wang, J. Two dimensional hexagonal boron nitride (2D-hBN): Synthesis, properties and applications. *J. Mater. Chem. C* **2017**, *5*, 11992–12022.

[43] Golberg, D.; Bando, Y.; Huang, Y.; Terao, T.; Mitome, M.; Tang, C. C.; Zhi, C. Y. Boron nitride nanotubes and nanosheets. *ACS Nano* **2010**, *4*, 2979–2993.

[44] Zeng, H. B.; Zhi, C. Y.; Zhang, Z. H.; Wei, X. L.; Wang, X. B.; Guo, W. L.; Bando, Y.; Golberg, D. "White graphenes": Boron nitride nanoribbons via boron nitride nanotube unwrapping. *Nano Lett.* 2010, *10*, 5049–5055.

[45] Zobelli, A.; Gloter, A.; Ewels, C. P.; Seifert, G.; Colliex, C. Electron knock-on cross section of carbon and boron nitride nanotubes. *Phys. Rev. B* **2007**, *75*, 245402.

[46] Zhang, Z. H.; Guo, W. L. Energy-gap modulation of BN ribbons by transverse electric fields: First-principles calculations. *Phys. Rev. B* **2008**, *77*, 075403.

[47] Barone, V.; Peralta, J. E. Magnetic boron nitride nanoribbons with tunable electronic properties. *Nano Lett.* **2008**, *8*, 2210–2214.

[48] Britnell, L.; Gorbachev, R. V.; Jalil, R.; Belle, B. D.; Schedin, F.; Katsnelson, M. I.; Eaves, L.; Morozov, S. V.; Mayorov, A. S.; Peres, N. M. R. et al. Electron tunneling through ultrathin boron nitride crystalline barriers. *Nano Lett.* **2012**, *12*, 1707–1710.

[49] Wang, Z. F.; Tang, Z. J.; Xue, Q.; Huang, Y.; Huang, Y.; Zhu, M. S.; Pei, Z. X.; Li, H. F.; Jiang, H. B.; Fu, C. X.; Zhi, C. Y. Fabrication of boron nitride nanosheets by exfoliation. *Chem. Rec.* **2016**, *16*, 1204–1215.

[50] Bao, J.; Jeppson, K.; Edwards, M.; Fu, Y. F.; Ye, L. L.; Lu, X. Z.; Liu, J. Synthesis and applications of two-dimensional hexagonal boron nitride in electronics manufacturing. *Electron. Mater. Lett.* **2016**, *12*, 1–16.
[51] Kibsgaard, J.; Tsai, C.; Chan, K.; Benck, J. D.; Nørskov, J. K.; Abild-Pedersen, F.; Jaramillo, T. F. Designing an improved transition metal phosphide catalyst for hydrogen evolution using experimental and theoretical trends. *Energy Environ. Sci.* **2015**, *8*, 3022–3029.
[52] Grahame, D. C. The electrical double layer and the theory of electrocapillarity. *Chem. Rev.* **1947**, *41*, 441–501.
[53] Kötz, R.; Carlen, M. Principles and applications of electrochemical capacitors. *Electrochim. Acta* **2000**, *45*, 2483–2498.
[54] Zhu, D.; Zhang, L. H.; Ruther, R. E.; Hamers, R. J. Photo-illuminated diamond as a solid-state source of solvated electrons in water for nitrogen reduction. *Nat. Mater.* **2013**, *12*, 836–841.
[55] Watt, G. W.; Chrisp, J. D. Spectrophotometric method for determination of hydrazine. *Anal. Chem.* **1952**, *24*, 2006–2008.
[56] Segall, M. D.; Lindan, P. J. D.; Probert, M. J.; Pickard, C. J.; Hasnip, P. J.; Clark, S. J.; Payne, M. C. First-principles simulation: Ideas, illustrations and the castep code. *J. Phys.: Condens. Matter* **2002**, *14*, 2717–2744.
[57] Perdew, J. P.; Chevary, J. A.; Vosko, S. H.; Jackson, K. A.; Pederson, M. R.; Singh, D. J.; Fiolhais, C. Atoms, molecules, solids, and surfaces: Applications of the generalized gradient approximation for exchange and correlation. *Phys. Rev. B* **1992**, *46*, 6671–6687.
[58] Blöchl, P. E. Projector augmented-wave method. *Phys. Rev. B* **1994**, *50*, 17953–17979.
[59] Grimme, S.; Antony, J.; Ehrlich, S.; Krieg, H. A consistent and accurate *ab initio* parametrization of density functional dispersion correction (DFT-D) for the 94 elements H-Pu. *J. Chem. Phys.* **2010**, *132*, 154104.
[60] Thangasamy, P.; Sathish, M. Supercritical fluid processing: A rapid, one-pot exfoliation process for the production of surfactant-free hexagonal boron nitride nanosheets. *CrystEngComm* **2015**, *17*, 5895–5899.
[61] Sun, W. L.; Meng, Y.; Fu, Q. R.; Wang, F.; Wang, G. J.; Gao, W. H.; Huang, X. C.; Lu, F. S. High-yield production of boron nitride nanosheets and its uses as a catalyst support for hydrogenation of nitroaromatics. *ACS Appl. Mater. Interfaces* **2016**, *8*, 9881–9888.
[62] Zhong, B.; Wu, Y.; Huang, X. X.; Wen, G. W.; Yu, H. M.; Zhang, T. Hollow BN microspheres constructed by nanoplates: Synthesis, growth mechanism and cathodoluminescence property. *CrystEngComm* **2011**, *13*, 819–826.
[63] Xu, Z. G.; Tian, H.; Khanaki, A.; Zheng, R. J.; Suja, M.; Liu, J. L. Large-area growth of multi-layer hexagonal boron nitride on polished cobalt foils by plasma-assisted molecular beam epitaxy. *Sci. Rep.* **2017**, *7*, 43100.
[64] Légaré, M. A.; Bélanger-Chabot, G.; Dewhurst, R. D.; Welz, E.; Krummenacher, I.; Engels, B.; Braunschweig, H. Nitrogen fixation and reduction at boron. *Science* **2018**, *359*, 896–900.
[65] Zhou, F. L.; Azofra, L. M.; Ali, M.; Kar, M.; Simonov, A. N.; McDonnell-Worth, C.; Sun, C. H.; Zhang, X. Y.; MacFarlane, D. R. Electro-synthesis of ammonia from nitrogen at ambient temperature and pressure in ionic liquids. *Energy Environ. Sci.* **2017**, *10*, 2516–2520.
[66] Xia, L.; Wu, X. F.; Wang, Y.; Niu, Z. G.; Liu, Q.; Li, T. S.; Shi, X. F.; Asiri, A. M.; Sun, X. P. S-doped carbon nanospheres: An efficient electrocatalyst toward artificial N_2 fixation to NH_3. *Small Methods* **2018**, *2*, 1800251.
[67] Kong, J. M.; Lim, A.; Yoon, C.; Jang, J. H.; Ham, H. C.; Han, J.; Nam, S.; Kim, D.; Sung, Y. E.; Choi, J.; Park, H. S. Electrochemical synthesis of NH_3 at low temperature and atmospheric pressure using a γ-Fe_2O_3 catalyst. *ACS Sustainable Chem. Eng.* **2017**, *5*, 10986–10995.
[68] Ren, X; Zhao, J. X.; Wei, Q.; Ma, Y. J.; Guo, H. R.; Liu, Q.; Wang, Y.; Cui, G. W.; Asiri, A. M.; Li, B. H.; Tang, B.; Sun, X. P. High-performance N_2-to-NH_3 conversion electrocatalyzed by Mo_2C nanorod. *ACS Cent. Sci.* **2019**, *5*, 116–121.
[69] Guo, C. X.; Zhang, L. Y.; Miao, J. W.; Zhang, J. T.; Li, C. M. DNA-functionalized graphene to guide growth of highly active Pd nanocrystals as efficient electrocatalyst for direct formic acid fuel cells. *Adv. Energy Mater.* **2013**, *3*, 167–171.
[70] Skúlason, E.; Bligaard, T.; Gudmundsdóttir, S.; Studt, F.; Rossmeisl, J.; Abild-Pedersen, F.; Vegge, T.; Jónssonac, H.; Nørskov, J. K. A theoretical evaluation of possible transition metal electro-catalysts for N_2 reduction. *Phys. Chem. Chem. Phys.* **2012**, *14*, 1235–1245.
[71] Zhao, J. X.; Chen, Z. F. Single Mo atom supported on defective boron nitride monolayer as an efficient electrocatalyst for nitrogen fixation: A computational study. *J. Am. Chem. Soc.* **2017**, *139*, 12480−12487.